

Analysis of *Gaia* Data Release 3 Parallax bias in the Galactic plane

Ye Ding^{1,2}, Shilong Liao^{1,2,*}, Qiqi Wu^{1,2}, Zhaoxiang Qi^{1,2}, and Zhenghong Tang^{1,2}

¹ Shanghai Astronomical Observatory, Chinese Academy of Sciences, Shanghai 200030, China

² University of Chinese Academy of Sciences, Beijing 100049, China

ABSTRACT

Context. The systematic errors are inevitable in *Gaia* published astrometric data. Lindegren et al. (L21) proposed a global recipe to correct for the GEDR3 parallax zero point offset, which did not consider the Galactic plane. The applicability of their correction model to the Galactic plane remains uncertain.

Aims. We attempt to have an independent investigation into the sample dependence of the L21 correction, and its applicability to the Galactic plane.

Methods. We collect various samples, including quasars, binaries, and sources with parallaxes from other surveys or methods, to validate the L21 correction, especially in the Galactic plane.

Results. We conclude that the L21 correction exhibits sample dependence, and does not apply effectively to the Galactic plane. We present a new parallax bias correction applying to the Galactic plane, offering improvements over the existing L21 correction. The correction difference between L21 and this work can go up to 10 μas within certain ranges of magnitude and colour. This work provides an additional recipe for users of *Gaia* parallaxes, especially for sources located near the Galactic plane.

Key words. astrometry – parallaxes – methods: data analysis – stars: distances

1. Introduction

The third data release from the European Space Agency mission *Gaia* covers observations made between July 2014 and May 2017, during the first 34 months of the *Gaia* mission (Gaia Collaboration et al. 2016, 2023b). It occurs in two stages: the early stage, *Gaia* Early Data Release 3 (GEDR3), which provides updated astrometry and photometry, supplemented by radial velocities from the second data release (*Gaia* Data Release 2, GDR2) (Gaia Collaboration et al. 2018); and the full *Gaia* Data Release 3 (GDR3), which includes the same sources as GEDR3 along with new radial velocities, spectra, light curves, astrophysical parameters, and more. The astrometric data in GDR3 are identical to those in GEDR3. In GDR3, the typical uncertainties of parallaxes range from 0.03 to 1.3 mas for stars with $15 < G < 21$ mag.

As one of the most critical data provided by the *Gaia* mission, high-precision, and high-accuracy parallaxes enable the derivation of reliable stellar distances. This has a significant impact on fields such as stellar formation and evolution, and the structure and dynamics of the Milky Way. However, systematic errors are inevitable in the published astrometric data because of imperfections in the instrument and data processing methods (Lindegren et al. 2021b). Several studies have investigated the parallax zero point offset of GEDR3 using different tracers, including quasars ($\sim -21 \mu\text{as}$, Lindegren et al. 2021b; $\sim -24 \mu\text{as}$, Liao et al. 2021), red giant stars ($\sim +22 \mu\text{as}$, Zinn 2021), red clump stars ($\sim +26 \mu\text{as}$, Huang et al. 2021) and W Ursae Majoris (EW)-type eclipsing binary systems ($\sim -27 \mu\text{as}$, Ren et al. 2021). Fabricius et al. (2021) compared the GEDR3 parallaxes with various external catalogues. With the use of external reference catalogues of open clusters (Kharchenko et al. 2013; Dias et al. 2014), they derived an average zero point difference of -59

μas and $-91 \mu\text{as}$, respectively. Lindegren et al. (2021a, hereafter L21) proposed a recipe to correct the GEDR3 parallax zero point offset, which is a function of G -band magnitude, colour information and ecliptic latitude of the sources. The correction functions are denoted as $Z_5(G, v_{\text{eff}}, \beta)$ and $Z_6(G, v_{\text{eff}}, \beta)$ for five-parameter and six-parameter solutions, respectively, where Z represents the parallax zero point offset. The colour parameter used in L21 correction is the (photometric) effective wavenumber in Z_5 , and the (astrometric) pseudocolour in Z_6 . The L21 correction is based on three samples: quasars in *Gaia*-CRF3 (hereafter GCRF3, Gaia Collaboration et al. 2022), stars in Large Magellanic Cloud, and binaries. Thus, the applicability of the L21 correction to other samples not considered in their model remains unknown. Additionally, the samples they considered are nearly devoid of targets in the Galactic plane due to the high source densities in this region. Consequently, the applicability of their correction model to the Galactic plane also remains uncertain because of the paucity of sources in this area.

The aim of this paper is to have an independent investigation into the sample dependence of the L21 correction, and its applicability to the Galactic plane. To achieve this, we have collected various samples within the Galactic plane. Quasars provide a direct estimate of the parallax bias, including data from the Large Sky Area Multi-Object Fibre Spectroscopic Telescope Data Release 10 (LAMOST DR10) (Jin et al. 2023), Sloan Digital Sky Survey Data Release 16 (SDSS DR16) (Lyke et al. 2020), Sixth Release of the Large Quasar Astrometric Catalogue (LQAC-6) (Souhay et al. 2024), the all-sky spectroscopic quasar catalogue - Quaia (Storey-Fisher et al. 2024), the quasar candidate catalogue behind the Galactic plane (GPQ) (Fu et al. 2021, 2022) and the improved *Gaia* DR3 quasar candidate catalogue, CatNorth, built with data from *Gaia*, Pan-STARRS1, and CatWISE2020 (Fu et al. 2024). In addition, wide binaries (El-Badry et al. 2021), which are so widely separated that the

* Corresponding author: Shilong Liao, shilongliao@shao.ac.cn

Table 1. Statistics of the cross-matches of GDR3 to external catalogues.

Catalogue	Sources	Unique matches		Filtered sources		Retained sources		Reference
		$ b \leq 20^\circ$	$ b > 20^\circ$	$ b \leq 20^\circ$	$ b > 20^\circ$	$ b \leq 20^\circ$	$ b > 20^\circ$	
SDSS DR16Q	750 414	2159	451 336	1851	386 161	53	4043	Lyke et al. (2020)
LAMOST DR10	83 376	2556	56 847	2005	54 743	155	609	Jin et al. (2023)
LQAC-6	1 149 138	73 460	1 072 290	73 452	1 070 332	-	262	Souchay et al. (2024)
Quaia	1 295 502	153 416	1 142 086	153 256	1 141 270	39 425	128 280	Storey-Fisher et al. (2024)
GPQ	100 153	100 104	-	100 087	-	20 468	-	Fu et al. (2021, 2022)
CatNorth	1 545 514	193 002	1 352 512	190 206	1 329 186	21 162	106 157	Fu et al. (2024)
KiDS DR4	157 813	-	74 478	-	56 074	-	2237	Nakoneczny et al. (2021)
Wide Binary	1 256 400	605 346	651 022	241 318	270 127	241 318	270 127	El-Badry et al. (2021)
VLBI	108	75	27	70	25	70	25	Xu et al. (2019)
HST	111	46	56	34	41	34	41	Groenewegen (2021)
Red Giant	12 500	6821	7704	6456	7237	6456	7237	Khan et al. (2023)
RR Lyrae	401	77	324	76	324	76	324	Muraveva et al. (2018)
Red Clump	137 448	96 813	37 666	91 929	36 508	91 929	36 508	Huang et al. (2020)
EW Binary	113 821	83 126	26 386	75 322	21 319	75 322	21 319	Ren et al. (2021)
RGB	44 784	37 199	7410	36 514	7220	36 514	7220	Hogg et al. (2019)

Notes. The external catalogues are listed in Col. 1. Column 2 shows the total number of sources in each catalogue. Columns 3-4 provide the number of unique matches in GDR3 for each catalogue. Columns 5-6 present the number of matched sources satisfying Eqs. (1)-(3) for quasars, stars, and binaries, respectively. Columns 7-8 show the number of sources retained after filtering. Column 9 provides references for the catalogues. A dash (-) indicates that the number of sources is zero.

two components never interact, have been considered to investigate the parallax bias. What's more, parallaxes from other surveys or methods are required to investigate the parallax offset by comparing them with the *Gaia* parallaxes, including (1) trigonometric parallaxes from the *Hubble* Space Telescope (HST) (Groenewegen 2021) and Very Long Baseline Interferometry (VLBI) astrometry (Xu et al. 2019), (2) RR Lyrae stars (RRLs) with the derived parallaxes from the recalibrated period-absolute magnitude-metallicity (PMZ) relations (Muraveva et al. 2018), (3) Red clump stars (RCs) with the derived parallaxes from recalibrated absolute magnitudes based on LAMOST data (Huang et al. 2020), (4) W Ursae Majoris (EW)-type eclipsing binary systems with the derived parallaxes from the recalibrated period-luminosity relation (Ren et al. 2021), (5) Red giant stars (RGs) with the asteroseismic parallaxes (Khan et al. 2023), and (6) Red-giant branch stars (RGBs) with the spectrophotometric parallaxes (Hogg et al. 2019).

The paper is structured as follows. Section 2 details the sample selection process. In Sect. 3, we validate the L21 correction using the samples described in Sect. 2. Section 4 presents a new estimate of the parallax correction coefficients applicable to the Galactic plane. In Sect. 5, we compare and validate two parallax bias corrections. The summary concludes the paper in Sect. 6.

2. Sample selection

To investigate the sample dependence of the L21 correction and its applicability to the Galactic plane, we require extensive and high-quality samples, including QSOs, wide binaries, and sources with parallaxes from other surveys or methods. Table 1 lists the result of cross-matches with 15 external catalogues located at $|b| \leq 20^\circ$ ¹ and $|b| > 20^\circ$ (b represents Galactic latitude), respectively, followed by further astrometric filtering.

¹ We select $|b| \leq 20^\circ$ rather than 10° for two reasons: first, to broaden our sample coverage and encompass a larger portion of the Galactic plane, and second, to ensure an overlapping area with GCRF3 which was considered in L21.

2.1. Cross-matching

First, we cross-match the GDR3 astrometric catalogue with the external catalogues listed in Table 1. The first seven entries in the table - SDSS DR16Q, LAMOST DR10, LQAC-6, Quaia, GPQ, CatNorth, and KiDS DR4 - are quasar catalogues. The eighth entry is the catalogue of binaries. Entries from the ninth to the last - VLBI, HST, RGs, RRLs, RCs, EWs, and RGBs - are sources with parallaxes from other surveys or methods. The astrometric information is used for the cross-matches. In cases where more than one *Gaia* source is matched to a source in the external catalogue, and vice versa, these sources are removed. We only consider unique matches in the case where one *Gaia* source is matched to one source in the external catalogue. Table 1 gives statistics of the cross-matches of GDR3 to external catalogues. Columns 3-4 list the number of unique matches located at $|b| \leq 20^\circ$ and $|b| > 20^\circ$ in GDR3, respectively. Further filtering, as described below, is then applied.

2.1.1. Quasars

Due to the high source densities in the Galactic plane, ensuring the cleanliness of the quasar sample is challenging. Lyke et al. (2020) presented the final SDSS-IV quasar catalogue from Data Release 16, containing 750 414 sources in their quasar-only sub-catalogue. We cross-match this catalogue with GDR3 by using the table 'gaiadr3.dr2_neighbourhood' in *Gaia* archive, applying matching conditions of 'angular_distance < 100 mas' and 'magnitude_difference < 0.5 mag'. This results in 2159 and 451 336 unique matches located at $|b| \leq 20^\circ$ and $|b| > 20^\circ$, respectively. Jin et al. (2023) provided the LAMOST quasar catalogue from Data Releases 1 to 10 which contains 83 376 sources. We cross-match the LAMOST quasar catalogue with GDR3 at a radius of 2 arcsec, in which the numbers of unique matches located at $|b| \leq 20^\circ$ and $|b| > 20^\circ$ are 2556 and 56 847, respectively. In addition, LQAC-6 presented by Souchay et al. (2024) contains 1 149 138 sources with high quasar probability (>0.9). We cross-match LQAC-6 with GDR3 at a radius of 1 arcsec and get 1 145

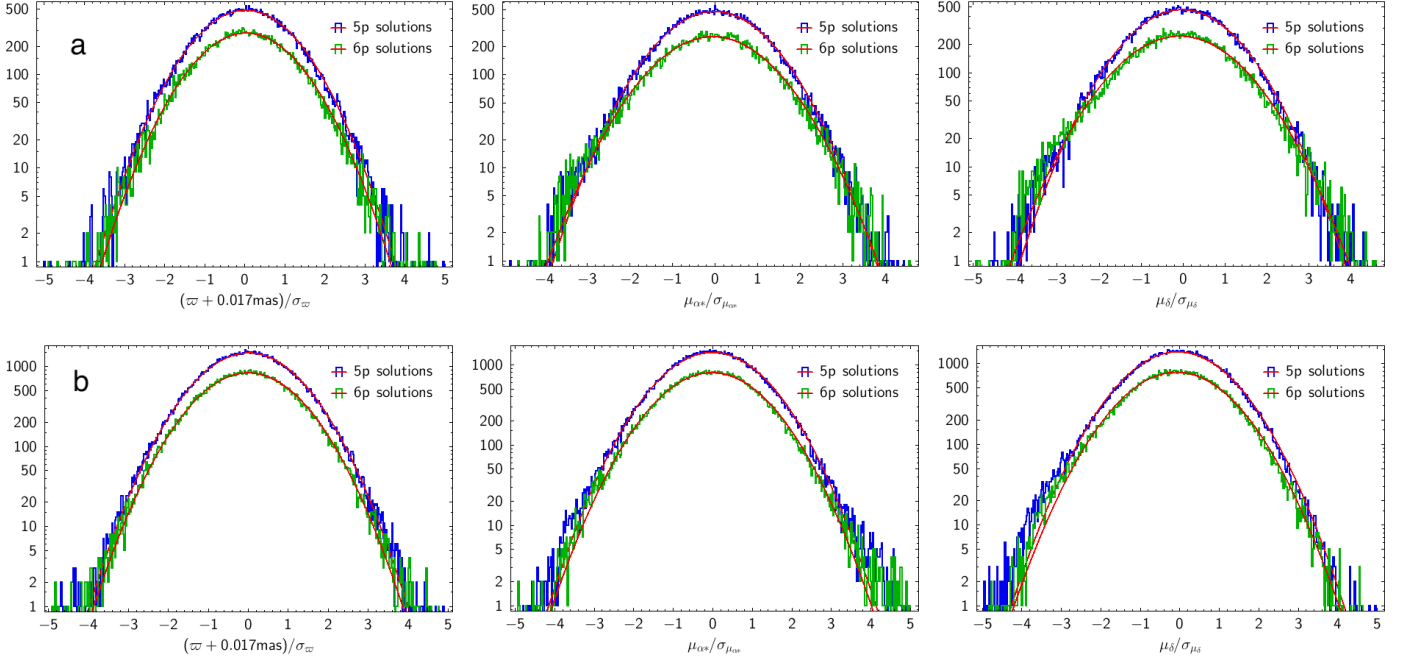


Fig. 1. Distributions of the normalised parallaxes and proper motion components for the Non-GCRF3 sample located at $|b| \leq 20^\circ$ (a) and $|b| > 20^\circ$ (b), respectively, with five-parameter (blue) and six-parameter (green) solutions. The turquoise curves show the corresponding best-fit Gaussian distributions.

750 unique matches. Among 1 145 750 matches, 73 460 and 1 072 290 sources are located at $|b| \leq 20^\circ$ and $|b| > 20^\circ$ respectively. Storey-Fisher et al. (2024) presented the all-sky quasar catalogue, Quaia, that samples the largest comoving volume of any existing spectroscopic quasar sample. They improved the quasar candidate catalogue identified by the *Gaia* mission with unWISE infrared data, applying cuts based on proper motions and colours. Their catalogue consists of 1 295 502 quasar candidates with $G < 20.5$, among which 153 416 and 1 142 086 sources are located at $|b| \leq 20^\circ$ and $|b| > 20^\circ$, respectively.

In addition, we consider quasar catalogues achieved by machine learning. Fu et al. (2021, 2022) provided a reliable GPQ candidate catalogue with 100 153 sources located at $|b| \leq 20^\circ$ achieved through a transfer-learning method for quasar selection, with the purity of $\sim 90\%$ on the Simbad matches. Among them, 100 104 unique matches are considered. Fu et al. (2024) presented CatNorth, an improved GDR3 quasar candidate catalogue, built with data from *Gaia*, Pan-STARRS1, and CatWISE2020. Their catalogue contains 1 545 514 reliable quasar candidates from the parent GDR3 quasar candidate catalogue. Among them, 193 002 and 1 352 512 sources are located at $|b| \leq 20^\circ$ and $|b| > 20^\circ$, respectively. What's more, the quasar catalogue from the Kilo-Degree Survey (KiDS) Data Release 4 with a purity of 97%, presented by Nakoneczny et al. (2021), includes 157 813 sources with high quasar probability ($p(\text{QSO}_{\text{cand}}) > 0.9$ for $r < 22$). We cross-match this catalogue with GDR3 at a radius of 2 arcsec, yielding 74 478 unique matches, all of which are located at $|b| > 20^\circ$.

2.1.2. Wide binaries

Similar to the approach in L21, we also consider binaries in our analysis. Physical binaries offer valuable insights into determining the parallax offset, as the binary components have essentially near-identical parallaxes. The catalogue of wide binaries (WBs)

of El-Badry et al. (2021) is listed in Table 1. In its raw form, it contains 1.8 million candidate physical binaries. The sample is restricted to the subset of 1 256 400 pairs with $>90\%$ probability of being bound (chance alignment $<10\%$). Among them, 605 346 and 651 022 pairs are located at $|b| \leq 20^\circ$ and $|b| > 20^\circ$, respectively, and further filtering will be described below.

2.1.3. Sources with parallaxes from other surveys or methods

See Table 1, initially, we consider independent trigonometric parallaxes. The VLBI astrometry is capable of measuring parallaxes with accuracies of $\sim 10 \mu\text{as}$ (Reid & Honma 2014), which has an astrometric quality comparable to that of GDR3. We cross-match 108 VLBI sources of Xu et al. (2019) with GDR3 at a radius of 100 mas, retaining 75 and 27 unique matches located at $|b| \leq 20^\circ$ and $|b| > 20^\circ$, respectively. In cases where one VLBI source has multiple reference parallaxes, we retain the one with higher precision (e.g., VY CMa, HD 283447, CoKu HP Tau G2, V1096 Tau, V1023 Tau, HD 283572, IRAS 20126+4104, HD 226868). Groenewegen (2021) compiled a list of 111 objects with the independent trigonometric parallax data from HST, considering the results determined by using the Fine Guidance Sensor (FGS) and the Wide Field Camera 3 (WFC3) from several studies (Benedict et al. 2017; van Belle et al. 2020; Bond et al. 2018; Riess et al. 2014, 2018; Casertano et al. 2016). We use the results of Groenewegen (2021) which provided GDR3 identifiers in their table. Of the 111 objects, only one object is not listed in GDR3 (Polaris A), and 8 objects have no parallax listed in GDR3. Among the left 102 objects, 46 and 56 unique matches are located at $|b| \leq 20^\circ$ and $|b| > 20^\circ$, respectively.

In addition to independent trigonometric parallaxes, derived parallaxes from different methods are also considered. First, independent distance measurements are available from astroseismology of red-giant stars. Khan et al. (2023) determined dis-

tances to nearly 12 500 RGs observed by Kepler, K2, and TESS. After cross-matching with GDR3 at a radius of 2 arcsec, 6821 and 7704 unique matches are located at $|b| \leq 20^\circ$ and $|b| > 20^\circ$, respectively.

Additionally, derived parallaxes making use of standard candles, distance indicators, and spectrophotometry are considered as well, including RRLs (Muraveva et al. 2018), RCs (Huang et al. 2020), EWs (Ren et al. 2021), and RGBs (Hogg et al. 2019). First, RRLs are radially pulsating stars used as standard candles for distance measurement. Muraveva et al. (2018) provided derived parallaxes for 401 RRLs based on recalibrated period-absolute magnitude-metallicity (PMZ) relations and absolute magnitude-metallicity relations. Among them, 77 and 324 RRLs are located at $|b| \leq 20^\circ$ and $|b| > 20^\circ$, respectively. Primary RCs are metal-rich low-mass stars (typically smaller than $2 M_\odot$) with stable luminosities, making them reliable distance indicators. Huang et al. (2020) presented a sample of 137 448 RCs with derived parallaxes. Using over 10 000 primary RCs with GDR2 parallaxes, they recalibrated the K_S absolute magnitudes based on LAMOST data, deriving distances for all RCs with this recalibration. The purity and completeness of their sample are generally higher than 80%. After cross-matching with GDR3 at a radius of 2 arcsec, 96 813 and 37 666 unique matches are located at $|b| \leq 20^\circ$ and $|b| > 20^\circ$, respectively. EWs can also serve as distance indicators due to their well-defined period-luminosity relationship. Ren et al. (2021) presented a catalogue of 113 821 EWs with derived parallaxes from the recalibrated period-luminosity relation. Among them, 83 126 and 26 386 EWs are located at $|b| \leq 20^\circ$ and $|b| > 20^\circ$ in GDR3, respectively. Hogg et al. (2019) determined spectrophotometric distances to 44 784 RGBs predicted with a data-driven model combining spectroscopy from APOGEE DR14 and photometric information from 2MASS, *Gaia*, and WISE. After cross-matching with GDR3 at a radius of 2 arcsec, 37 199 and 7410 unique matches are located at $|b| \leq 20^\circ$ and $|b| > 20^\circ$, respectively. The distance indicator calibrations of RRLs, RCs, EWs, and RGBs, as mentioned above, indirectly depend on *Gaia* DR2 or DR3 parallaxes, making it potentially circular to use them for verifying GDR3 parallaxes. Therefore, it is important to note that these sources can not be considered independent checks. However, they remain valuable for investigating parallax zero-point differences as a function of colour and sky position.

2.2. Quality filtering

2.2.1. Quasars

For all quasar catalogues in Table 1, we apply the following criteria, which are adopted from the GCRF3 quasar selection (Gaia Collaboration et al. 2022).

$$\left\{ \begin{array}{l} \text{(i)} \quad \text{astrometric_params_solved} = 31 \quad \text{or} \quad 95, \\ \text{(ii)} \quad |(\varpi + 0.017 \text{ mas})| / \sigma_\varpi < 5, \\ \text{(iii)} \quad X_\mu^2 \equiv [\mu_{\alpha*} \quad \mu_\delta] \text{Cov}(\mu)^{-1} \begin{bmatrix} \mu_{\alpha*} \\ \mu_\delta \end{bmatrix} < 25 \end{array} \right. \quad (1)$$

Criterion (i) selects the sources that have five- or six-parameter astrometric solutions; Criterion (ii) takes the global parallax zero point offset of EDR3 ($-17 \mu\text{as}$) (Lindgren et al. 2021a) into account; Criterion (iii) is that the proper motion components $\mu_{\alpha*}$ and μ_δ should be small compared to their uncertainties $\sigma_{\mu_{\alpha*}}$ and σ_{μ_δ} , where $\text{Cov}(\mu)^{-1}$ is the covariance matrix of proper motion. The numbers of unique matches that survived the filtering by

Eq. (1) are provided in Cols. 5-6 of Table 1. This filtering resulted in the removal of 14%, 22%, 0.01%, 0.1%, 0.02%, and 1% of sources for SDSS DR16Q, LAMOST DR10, LQAC-6, Quiaia, GPQ, and CatNorth within the Galactic plane, respectively, and 14%, 4%, 0.2%, 0.07%, 2% and 25% of sources for SDSS DR16Q, LAMOST DR10, LQAC-6, Quiaia, CatNorth, and KiDS DR4 outside the Galactic plane, respectively.

2.2.2. Wide binaries

It can be assumed that the components of binaries have similar true parallaxes, although their magnitudes and colours may be very different. Thus, the parallax differences between the components of binaries should be as close to zero as possible. For the WBs, we applied the following criteria.

$$\left\{ \begin{array}{l} \text{(i)} \quad \text{astrometric_params_solved}_{1,2} = 31 \quad \text{or} \quad 95 \\ \text{(ii)} \quad |(\varpi_1 - \varpi_2)| / \sqrt{\sigma_{\varpi_1}^2 + \sigma_{\varpi_2}^2} < 5 \\ \text{(iii)} \quad 16.1 \leq G_2 < 21.0 \end{array} \right. \quad (2)$$

where ‘1’ and ‘2’ denote the components with the brighter and fainter G magnitudes, respectively. Criterion (i) selects WBs whose components both have five- or six-parameter astrometric solutions. Criterion (ii) selects WBs whose parallax differences between two components fall within five times the formal uncertainty. Criterion (iii) selects WBs whose fainter components can be corrected using the quasar-derived recipe (see Sect. 4). The numbers of unique matches that survived the filtering by Eq. (2) are listed in Cols. 5-6 of Table 1, resulting in the removal of 60% and 59% of pairs within and outside the Galactic plane, respectively.

2.2.3. Sources with parallaxes from other surveys or methods

First, for sources with parallaxes from other surveys or methods in Table 1, we applied the criteria (i) in Eq. (1) to select the sources that have five- or six-parameter astrometric solutions. We assume that the parallax offsets ($\Delta\varpi$) of these sources are given by the difference between GDR3 parallax (ϖ_G) and other parallax determinations (ϖ_O). Assuming that errors are Gaussian as given in GDR3, we use the following criteria to select sources,

$$|(\varpi_G - \varpi_O)| / \sqrt{\sigma_{\varpi_G}^2 + \sigma_{\varpi_O}^2} < 5 \quad (3)$$

where the parallax difference of the source should be zero within five times the formal uncertainty. The numbers of unique matches of sources that survived the filtering by Eq. (1-i) and Eq. (3) are given in Cols. 5-6 of Table 1, removing 7%, 26%, 1%, 7%, 9%, 5%, and 2% of sources within the Galactic plane, and 7%, 27%, 0, 3%, 19%, 6%, and 3% of sources outside the Galactic plane, for VLBI, HST, RRLs, RCs, EWs, RGs, and RGBs, respectively.

2.3. Final selection

The numbers of the retained sources are given in Cols. 7-8 of Table 1. For WBs, all filtered sources are retained, with 63% having five-parameter solutions and 37% having six-parameter solutions. For sources with parallaxes from other surveys or methods, all filtered sources are also retained, with 98% having five-parameter solutions and 2% having six-parameter solutions. For all quasar catalogues, we first exclude overlapping

sources in GCRF3 to obtain the Non-GCRF3 sources. Next, duplicate Non-GCRF3 sources among quasar catalogues are removed. The final union of the Non-GCRF3 sample contains 81 263 sources located at $|b| \leq 20^\circ$ and 241 588 sources at $|b| > 20^\circ$. Among the Non-GCRF3 sources within the Galactic plane, 51 546 (63%) have five-parameter solutions and 29 717 (37%) have six-parameter solutions in GDR3. Outside the Galactic plane, 153 923 (64%) have five-parameter solutions and 87 665 (36%) have six-parameter solutions in GDR3.

To estimate the level of stellar contamination in Non-GCRF3, we analysed histograms of the normalised parallaxes ϖ/σ_ϖ and normalised proper motion components $\mu_{\alpha*}/\sigma_{\mu_{\alpha*}}$ and $\mu_\delta/\sigma_{\mu_\delta}$. Ignoring small systematic and random offsets, the normalised quantities should follow Gaussian distributions with mean values close to zero and standard deviations only slightly larger than one for a clean sample of QSOs, as described in [Gaia Collaboration et al. \(2022\)](#) (see Sect. 2.3). Conversely, if their distributions deviate significantly from the expected Gaussian, it indicates that the sample is contaminated by stellar objects with non-zero parallaxes and/or proper motions. Figure 1 shows the distributions of the normalised parallaxes and proper motion components for the Non-GCRF3 sample located at $|b| \leq 20^\circ$ and $|b| > 20^\circ$, respectively, with five-parameter and six-parameter solutions. For the Non-GCRF3 sample located at $|b| \leq 20^\circ$, the standard deviations of the three normalised quantities are 1.058, 1.075, and 1.098 for the five-parameter solutions and 1.071, 1.158, and 1.210 for the six-parameter solutions. For the Non-GCRF3 sample located at $|b| > 20^\circ$, the standard deviations are 1.042, 1.087, and 1.107 for the five-parameter solutions and 1.053, 1.105, and 1.127 for the six-parameter solutions. In comparison, the standard deviations of the normalised quantities in GCRF3 are 1.052, 1.055, and 1.063 for the five-parameter solutions and 1.073, 1.099, and 1.116 for the six-parameter solutions ([Gaia Collaboration et al. 2022](#)). The slightly larger standard deviations in our Non-GCRF3 sample indicate minor differences, but overall, the distributions remain very symmetric and close to Gaussian, suggesting a low level of stellar contamination.

Due to the high density of stellar sources in the Galactic plane, we also plot the colour-colour diagram for the Non-GCRF3 sample located at $|b| \leq 20^\circ$, compared with galaxies, stars, and GCRF3 located at $|b| \leq 20^\circ$, see Fig. 2. For the Non-GCRF3 sample, we sample 2000 quasars to better visualise the overlapping structures with GCRF3. The selection of galaxies and stars used in the analysis are detailed in Appendix A. The overlap between the contours of the Non-GCRF3 and GCRF3 samples indicates the reliability of our sample. Figure 3 displays the distribution of the Non-GCRF3 sample located at $|b| \leq 20^\circ$ in Galactic latitude. In this paper, we focus on sources with five-parameter solutions, as most of our samples have five-parameter solutions.

3. Validation of the L21 correction

In this section, we assess the validity of the L21 correction by dividing the sky into two regions: the Galactic plane region ($|b| \leq 20^\circ$) and the off-Galactic plane region ($|b| > 20^\circ$). We use QSOs, WBs, and sources with parallaxes from other surveys or methods listed in Table 1 to evaluate the L21 correction.

3.1. Quasar verification

First, we use quasars to assess the validity of the L21 correction. Since the L21 correction is primarily based on the GCRF3 sam-

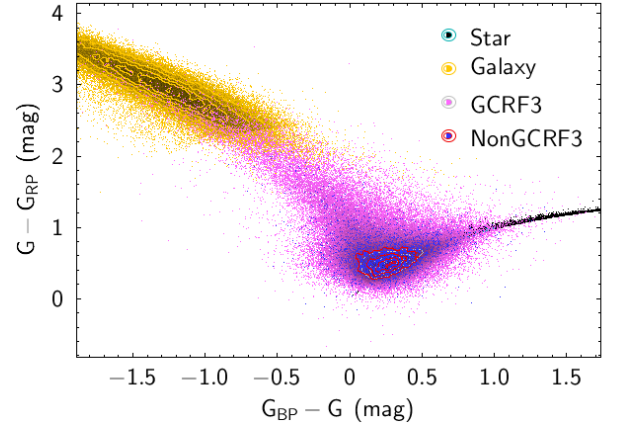


Fig. 2. Colour-colour diagram for Non-GCRF3 (blue), GCRF3 (pink), and galaxies (yellow) as well as stars (black) in the Galactic plane ($|b| \leq 20^\circ$).

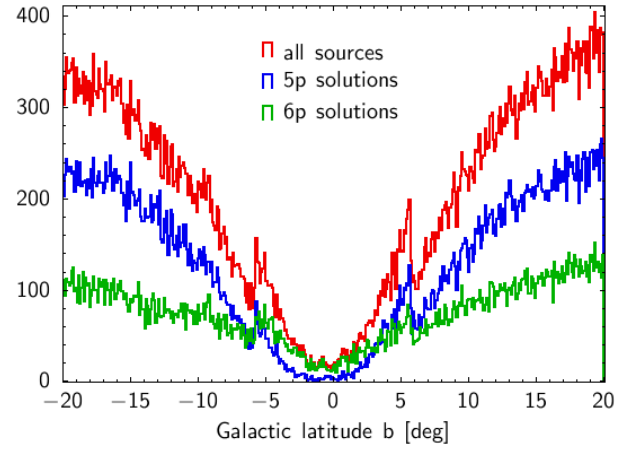


Fig. 3. Distribution of the Non-GCRF3 sample located at $|b| \leq 20^\circ$ in Galactic latitude. The distribution is shown for the whole sample (red) and separately for the sources with five-parameter (blue) and six-parameter (green) astrometric solutions.

ple, we apply it to the Non-GCRF3 sample to examine its sample dependence.

Figures 4 and 5 display the results for the five-parameter solutions of the Non-GCRF3 sample located at $|b| \leq 20^\circ$ and $|b| > 20^\circ$, respectively. The figures are divided according to magnitude, colour, and ecliptic latitude. Blue dots show the individual values plotted versus magnitude, effective wavenumber, and sine of ecliptic latitude. Black circles show mean values of the uncorrected parallaxes (ϖ) in bins of magnitude etc.; green circles show mean values of the corrected parallaxes ($\varpi - Z_5$) applying the L21 correction. In Fig. 4, the corrected parallaxes (green) are not centred on zero, showing a zero-point deviation of approximately $20 \mu\text{as}$. It indicates that the L21 correction does not apply to the Galactic plane effectively. In contrast, Fig. 5 shows that the L21 correction is more effective for sources located at $|b| > 20^\circ$, particularly in regions of high source densities.

3.2. Binary verification

It can be assumed that the components of binaries have similar true parallaxes, although their magnitudes and colours may be very different. We compare the corrected parallax differences

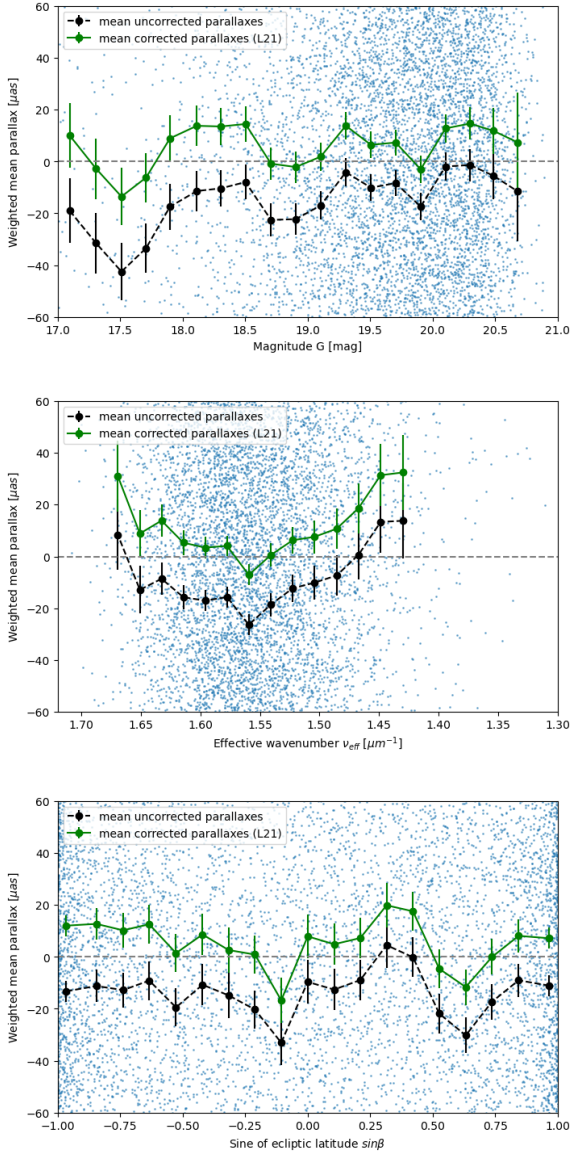


Fig. 4. Parallaxes for 51 546 quasars with five-parameter solutions located at $|b| \leq 20^\circ$ in the Non-GCRF3 sample.

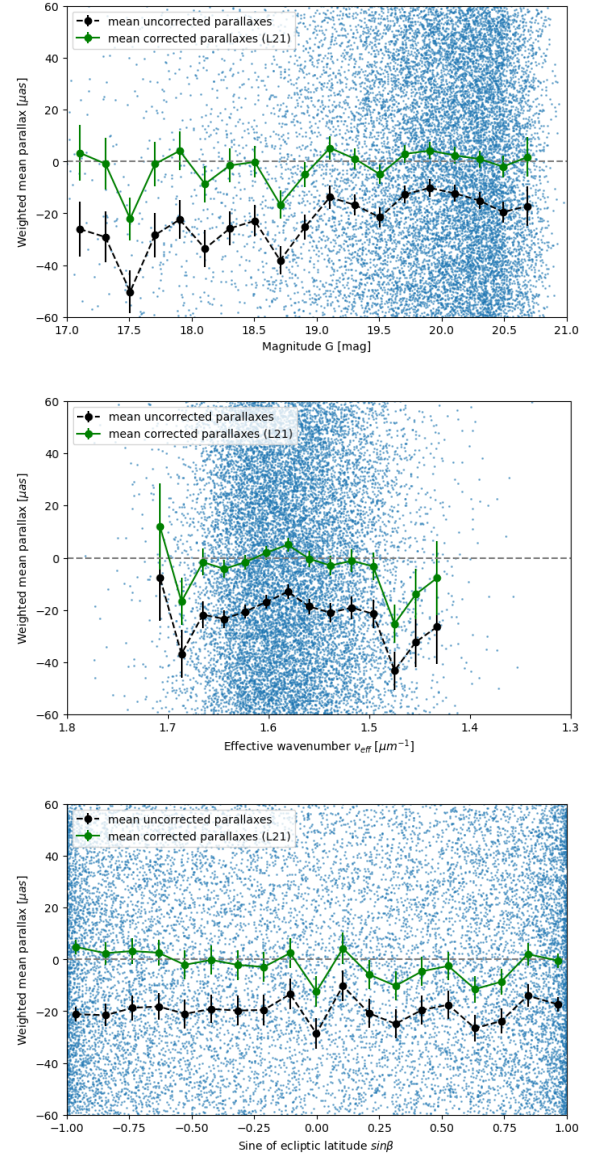


Fig. 5. Parallaxes for 153 923 quasars with five-parameter solutions located at $|b| > 20^\circ$ in the Non-GCRF3 sample.

(applying the L21 correction) of WBs with the zero point to check the validity of the L21 correction.

Figures 6 and 7 show the parallax differences for the five-parameter solutions of WBs located at $|b| \leq 20^\circ$ and $|b| > 20^\circ$, respectively, divided according to magnitude, colour, and ecliptic latitude. The horizontal axes represent the properties of the bright components of the binaries. Blue dots show the individual values plotted versus magnitude, effective wavenumber, and sine of ecliptic latitude. Black circles show mean values of the uncorrected parallax differences ($\varpi_1 - \varpi_2$) in bins of magnitude etc.; green circles show mean values of the corrected parallax differences applying the L21 correction ($(\varpi_1 - Z_{51}) - (\varpi_2 - Z_{52})$). After applying the L21 correction, the mean values of parallax differences (green) of WBs are not centred on zero, regardless of whether WBs are located at $|b| \leq 20^\circ$ or $|b| > 20^\circ$. We conclude that the L21 correction exhibits sample dependence and does not apply effectively to these WBs. The parallax differences as a function of magnitude and colour differences are shown in Appendix B. As expected, these differences approach zero for

small magnitude and colour differences for both the corrected and uncorrected versions.

3.3. Other verification

In addition to quasar and binary verifications, we also compare independent parallaxes from other surveys or methods with the GDR3 parallaxes to assess the validity of the L21 correction, including VLBI, HST, and RG sources listed in Table 1. Table 2 gives the results for five-parameter solutions of these sources located at $|b| \leq 20^\circ$ and $|b| > 20^\circ$, respectively. In the Galactic plane ($|b| \leq 20^\circ$), the L21 correction results in overcorrection for VLBI sources. Outside the Galactic plane ($|b| > 20^\circ$), the L21 correction results in overcorrection for VLBI, HST, and RG sources. For VLBI and HST sources, the sample sizes are too small to assess the L21 correction firmly. Based on these results, we conclude that the L21 correction exhibits sample dependence.

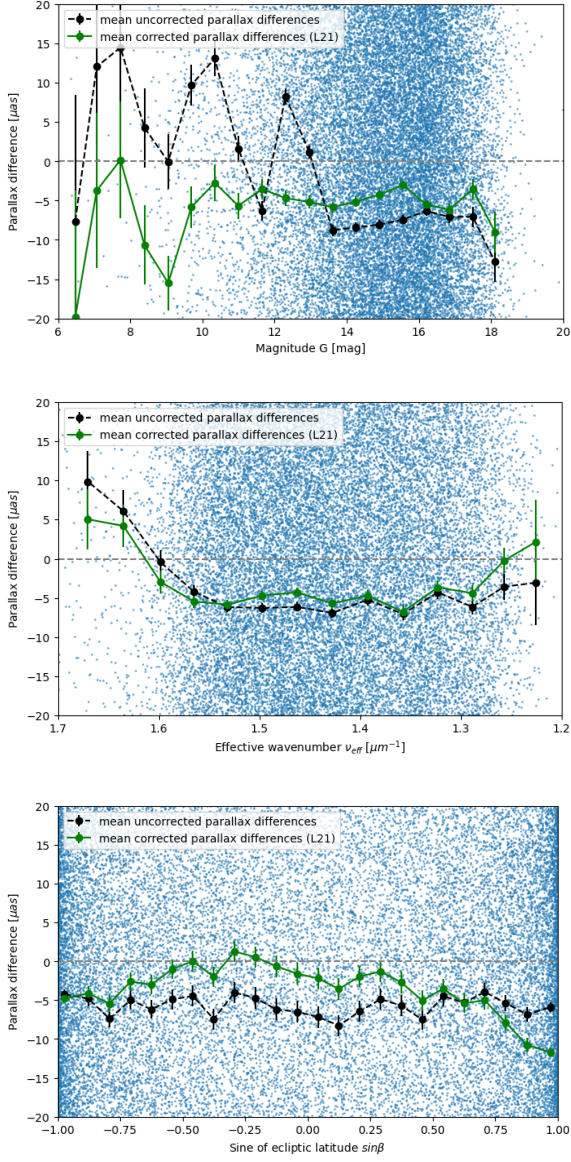


Fig. 6. Parallax differences of 148 234 binaries located at $|b| \leq 20^\circ$ with five-parameter solutions binned by magnitude, colour, and ecliptic latitude of the bright components of binaries.

Although RRLs, RCs, EWs, and RGBs cannot be considered independent checks due to their indirect dependence on *Gaia* parallaxes, we still present the results for these sources in Table 2. Additionally, we plot the parallax zero-point differences as a function of colour and ecliptic latitude for sources with derived parallaxes (RGs, RRLs, RCs, EWs, and RGBs) in Figure C.1. Details see Appendix C. Overall, the parallax zero-point differences show distinct behaviours within and outside the Galactic plane, suggesting the necessity of this work.

4. Estimate of the new correction coefficients

In this section, we fit the parallax bias function for sources with five-parameter solutions and get the new coefficients applying to the Galactic plane, primarily based on parameterised function $Z(G, \nu_{eff}, \beta)$ defined in L21 Appendix A. The generic function

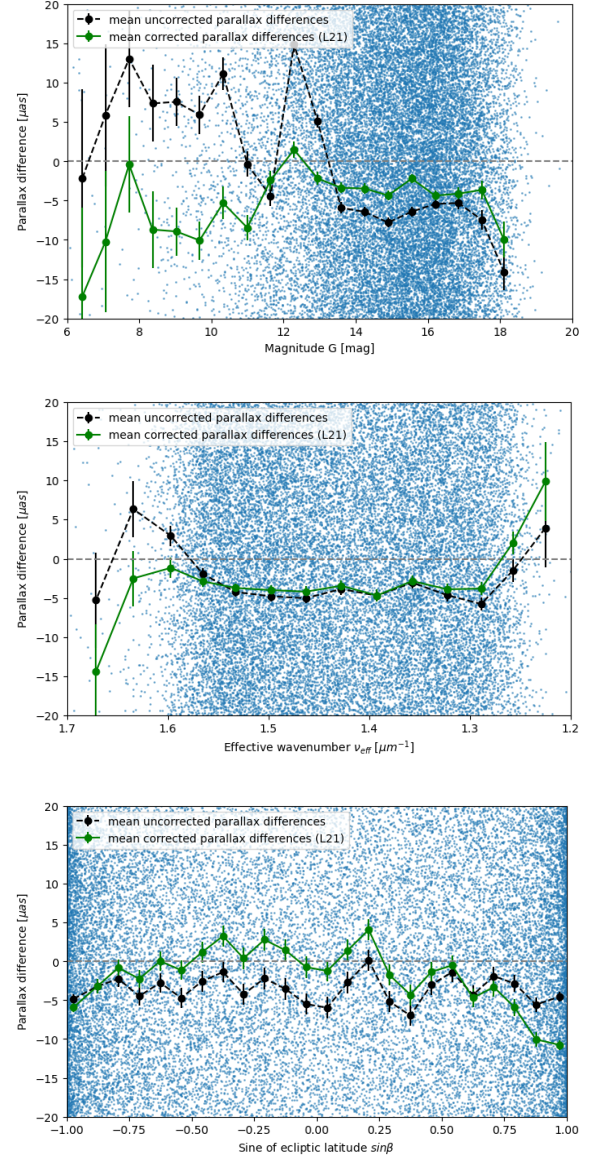


Fig. 7. Parallax differences of 172 931 binaries located at $|b| > 20^\circ$ with five-parameter solutions binned by magnitude, colour, and ecliptic latitude of the bright components of binaries.

is

$$Z(G, \nu_{eff}, \beta) = \sum_j \sum_k q_{jk}(G) c_j(\nu_{eff}) b_k(\beta) \quad (4)$$

where the functions

$$q_{jk}(G) = \sum_i z_{ijk} g_i(G), \quad j = 0 \dots 4, \quad k = 0 \dots 2 \quad (5)$$

are piecewise linear in G . Among the functions, $g_i(G)$ are the basis functions in magnitude, $c_j(\nu_{eff})$ are the basis functions in colour, and $b_k(\beta)$ are the basis functions in ecliptic latitude. The coefficients z_{ijk} are the free parameters used to fit Z to the given data. For more details on the basis functions, see L21 Appendix A.

The primary methods for estimating the new correction are: (i) using quasars to directly estimate the parallax bias for $G \gtrsim 16$, and (ii) using binaries to map differential variations for bright stars.

Table 2. Parallax corrections for sources with parallaxes with five-parameter solutions.

Catalogue	$ b \leq 20^\circ$			$ b > 20^\circ$		
	$\Delta\varpi$ (uncorrected parallax offset) (μas)	L21 correction (μas)	N	$\Delta\varpi$ (uncorrected parallax offset) (μas)	L21 correction (μas)	N
VLBI	-8.22	+21.5	32	+13.06	+33.26	9
HST	-22.96	+1.43	16	+111.93	+137.58	24
Red Giant	-19.15	+2.21	6300	-15.94	+8.20	6859
RR Lyrae	-31.76	-1.92	74	-30.33	+1.55	303
Red Clump	-25.98	+4.64	90 452	-20.65	+7.51	35 484
EW binary	-19.30	+14.87	75 296	-15.69	+18.61	21 317
RGB	-19.21	+9.97	27426	-25.86	+0.43	6989

Notes. Column 1 gives the name of catalogue. Columns 2-4 and 5-7 present the results for sources located at $|b| \leq 20^\circ$ and $|b| > 20^\circ$, respectively. Columns 2 and 5 show the weighted mean of the offset between the observed GDR3 parallaxes and parallaxes from other surveys or methods. Columns 3 and 6 give the weighted mean of the L21 correction. Columns 4 and 7 indicate the number of sources with five-parameter solutions.

4.1. Quasars

First, the Non-GCRF3 sample with five-parameter solutions located at $|b| \leq 20^\circ$ is used to estimate the new correction coefficients. For completeness, we also consider GCRF3 in the estimation. The GCRF3 sample located at $|b| \leq 20^\circ$ contains 139 907 sources with five-parameter solutions. The combined sample includes 191 286 sources with five-parameter solutions and wavenumbers in the range 1.24 to $1.72 \mu\text{m}^{-1}$. The magnitudes range from $G \simeq 13.8$ to 21.0; only 99 are brighter than $G = 16.1$.

Figure 8 shows the weighed mean parallax plotted against G , v_{eff} , β . The blue points show the parallaxes of individual sources. In each bin, the black square is the mean parallax in DR3 weighted by σ_ϖ^{-2} , with error bars indicating the estimated standard deviation of the weighted mean. The main trends are as follows.

- Overall, a negative parallax bias is observed: the weighted mean parallax of the sample is approximately $-18 \mu\text{as}$, with a median of about $-12.7 \mu\text{as}$. These values are represented by the red lines in Fig. 8, and they are slightly smaller than those reported in L21 (-21 and $-17 \mu\text{as}$).
- As a function of G , there is a non-linear variation when $G \lesssim 16$, followed by an approximately linear increase from $G \simeq 16$ to 20.
- The variation as a function of v_{eff} shows an approximately linear trend within the well-populated range of colours.
- As a function of β , there is a non-linear variation.

The trends described above can be well approximated by the parameterised function $Z(G, v_{\text{eff}}, \beta)$ in Eq. (5). However, considering the limited support in G and v_{eff} , we need to add some constraints. We only use $i = 8 \dots 12$ for the basis function in magnitude, $g_i(G)$, for the scarcity of quasars in the range $G < 16.1$. Additionally, for the basis function in colour, $c_j(v_{\text{eff}})$, we use $j = 0$ and 1 for wavenumbers of the sample in the range 1.24 to $1.72 \mu\text{m}^{-1}$. The quasar sample contains few sources redder than $v_{\text{eff}} \simeq 1.4 \mu\text{m}^{-1}$ or bluer than $1.7 \mu\text{m}^{-1}$, and therefore cannot be used to estimate q_{jk} for $j = 2, 3$, and 4.

Our estimate of $Z_5(G, v_{\text{eff}}, \beta)$ from the quasar sample is given by the coefficients q_{jk} in Table 3. It is primarily valid within the subspace populated by quasars. Most importantly, this does not include sources that are brighter than $G \simeq 16$ or redder than $v_{\text{eff}} \simeq 1.48 \mu\text{m}^{-1}$. To extend Z_5 in these directions, we resort to the differential method using physical pairs.

Table 3. Coefficients for the function fitted to the quasar parallaxes.

G	q_{00}	q_{01}	q_{02}	q_{10}	q_{11}	q_{12}
16.1	-28.46	+16.35	-39.53	+47.80	-159.86	+136.25
17.5	-20.79	-6.36	-2.21	-55.98	+41.07	-20.35
19.0	-11.49	+4.50	-1.85	-45.32	-26.16	+5.02
20.0	-5.03	-0.69	-5.61	-57.69	+49.24	+76.35
21.0	-2.29	-2.01	+51.04	-112.23	+123.50	-261.33

Notes. The table gives $q_{jk}(G)$ at the values of G in the first column. For other values of G , linear interpolation should be used. Units are: μas (for q_{0k}) and $\mu\text{as } \mu\text{m}$ (q_{1k}).

4.2. Wide binaries

Having mapped $Z_5(G, v_{\text{eff}}, \beta)$ for $G > 16.1$ by the mean of quasars, we extend our analysis to brighter sources. Similar to the methods in L21, we also use binaries, in which it can be assumed that the components share similar true parallaxes. Using the results from the previous section to ‘anchor’ the parallax bias of the fainter component of binaries, we can then estimate the bias of the brighter component, as shown in Eq. (6).

$$Z_5(G_1, v_{\text{eff}1}, \beta) = \varpi_1 - \varpi_2 + Z_5(G_2, v_{\text{eff}2}, \beta) \quad (6)$$

where ‘1’ and ‘2’ denote the components with the brighter and fainter G magnitude of binaries respectively, and $Z_5(G_2, v_{\text{eff}2}, \beta)$ represents the parallax bias of the faint component, with Z_5 defined by the coefficients in Table 3. The bias-corrected parallax of the faint component is computed as $\varpi_2 - Z_5(G_2, v_{\text{eff}2}, \beta)$, where ϖ_2 and $v_{\text{eff}2}$ are the published GDR3 parallax and effective wavenumber of the faint component. $Z_5(G_1, v_{\text{eff}1}, \beta)$ is denoted as the parallax bias estimate of the brighter component. We use WBs listed in Table 1 with five-parameter solutions and G in the range of 6.0 to 21.0, located at $|b| \leq 20^\circ$, to estimate the new correction coefficients.

Figure 9 shows the parallax bias of the bright components plotted against G , v_{eff} , β . The blue points show the parallax differences of individual sources. In each bin, the black square is the weighed mean parallax difference in DR3 weighted by σ_ϖ^{-2} , with error bars indicating the estimated standard deviation of the weighted mean. The main trends are as follows.

- In general, there is a negative parallax bias: the weighted mean parallax of the sample is approximately $-31.3 \mu\text{as}$, with a median of about $-29.1 \mu\text{as}$, as indicated by the two overlapping red lines in Fig. 9.

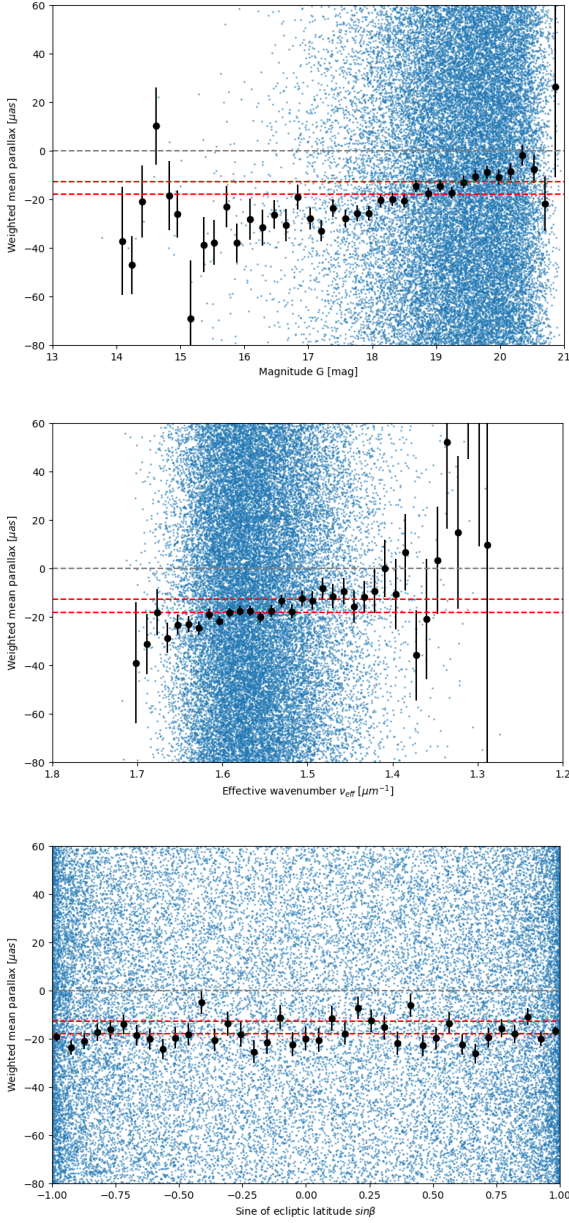


Fig. 8. Mean parallax of quasars binned by magnitude, effective wavenumber, and sine of ecliptic latitude. The two red lines indicate the weighted mean value ($-18 \mu\text{as}$) and median ($-12.7 \mu\text{as}$) of the full sample.

- As a function of G , there is a non-linear variation, except an approximately linear increase from $G \simeq 16$ to 18 .
- As a function of ν_{eff} , the variation is approximately linear when $\nu_{\text{eff}} \gtrsim 1.5$ and $\lesssim 1.7 \mu\text{m}^{-1}$, with a slight curvature when $\nu_{\text{eff}} \gtrsim 1.2$ and $\lesssim 1.5 \mu\text{m}^{-1}$. The sources are very few when $\nu_{\text{eff}} \gtrsim 1.7 \mu\text{m}^{-1}$.
- As a function of β , the variation can be described by a quadratic polynomial in $\sin\beta$.

The investigated magnitude interval overlaps with the range in Table 3 for $G \simeq 16.1$ to 19 , providing a consistency check and potentially improved estimate of the parallax bias in an interval poorly covered by quasars. Considering the trends in Fig. 9, We use $i = 0 \dots 10$ for the magnitude basis function, $g_i(G)$, and $j = 0, 1, 2$ for the colour basis function, $c_j(\nu_{\text{eff}})$. The curvature with colour in the mid-red region ($\nu_{\text{eff}} = 1.24$ to $1.48 \mu\text{m}^{-1}$) is fully

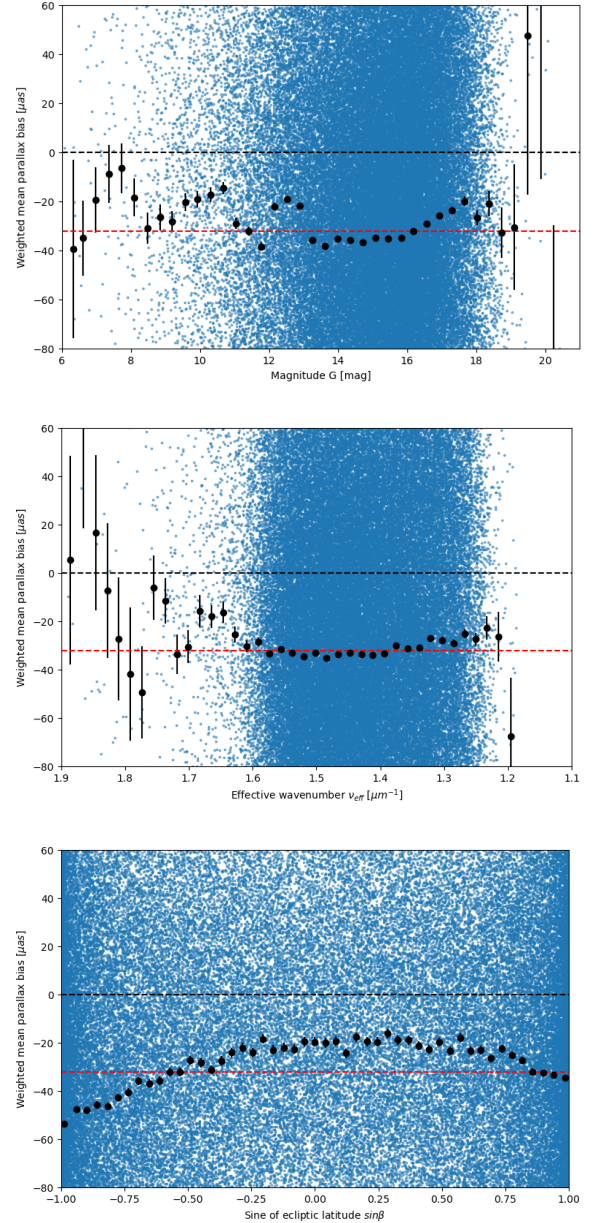


Fig. 9. Weighed mean parallax bias of the bright components of binaries binned by magnitude, effective wavenumber, and sine of ecliptic latitude. The two overlapping red lines indicate the weighted mean ($-31.3 \mu\text{as}$) and median ($-29.1 \mu\text{as}$) of the full sample.

described by the non-interaction term q_{20} , that is $q_{21} = q_{22} = 0$. A severe limitation is that the scarcity of bright sources with $\nu_{\text{eff}} < 1.2$ or $> 1.7 \mu\text{m}^{-1}$ makes it practically impossible to determine q_{30} and q_{40} . The resulting fit is given in Table 4.

4.3. Combined fit

The magnitude intervals overlap between Table 3 and 4 for $G = 16.1$ to 19.0 . We combine the coefficients for $G = 16.1$ to 21.0 from Table 3 and the coefficients for $G = 6.0$ to 15.9 from Table 4. After testing, this combination demonstrates effective corrections. The end result is shown in Table 5, which is our final estimate of the bias function for five-parameter solutions applying to the Galactic plane.

Table 4. Coefficients for the function as estimated from wide binaries.

G	q_{00}	q_{01}	q_{02}	q_{10}	q_{11}	q_{12}	q_{20}
6.0	-17.82	+18.56	-31.07	-53.63	+149.36	-298.61	-4877.35
10.8	-13.26	+13.52	-30.77	+20.86	-10.82	+53.55	-2412.08
11.2	-23.51	+9.61	-32.61	-73.44	+88.29	-14.61	+13501.35
11.8	-31.06	+16.19	-27.02	-44.66	-27.31	+44.23	-4053.40
12.2	-9.10	+13.07	-30.86	-95.25	+18.22	+97.42	+5590.58
12.9	-11.70	+17.77	-34.43	-38.31	-83.65	+16.80	+56.79
13.1	-30.48	+15.50	-31.92	-7.78	-67.85	+16.60	-272.16
15.9	-33.38	+6.62	-20.93	-82.04	-48.82	+43.17	-2002.14
16.1	-35.26	+3.76	-18.14	-115.44	-50.20	+49.47	-1960.32
17.5	-44.82	-14.78	-2.64	-237.22	-31.98	-41.61	-1560.55
19.0	-39.90	+38.81	-18.97	+66.18	+37.32	-143.85	+3162.85

Notes. The table gives $q_{jk}(G)$ at the values of G in the first column. For other values of G , linear interpolation should be used. Units are: μas (for q_{0k}) and $\mu as \mu m$ (q_{1k}).

Table 5. Final coefficients of $Z_5(G, v_{eff}, \beta)$ obtained by joining the results in Table 3 and Table 4.

G	q_{00}	q_{10}	q_{20}	q_{10}	q_{11}	q_{12}	q_{20}
6.0	-17.82	+18.56	-31.07	-53.63	+149.36	-298.61	-4877.35
10.8	-13.26	+13.52	-30.77	+20.86	-10.82	+53.55	-2412.08
11.2	-23.51	+9.61	-32.61	-73.44	+88.29	-14.61	+13501.35
11.8	-31.06	+16.19	-27.02	-44.66	-27.31	+44.23	-4053.40
12.2	-9.10	+13.07	-30.86	-95.25	+18.22	+97.42	+5590.58
12.9	-11.70	+17.77	-34.43	-38.31	-83.65	+16.80	+56.79
13.1	-30.48	+15.50	-31.92	-7.78	-67.85	+16.60	-272.16
15.9	-33.38	+6.62	-20.93	-82.04	-48.82	+43.17	-2002.14
16.1	-28.46	+16.35	-39.53	+47.80	-159.86	+136.25	-
17.5	-20.79	-6.36	-2.21	-55.98	+41.07	-20.35	-
19.0	-11.49	+4.50	-1.85	-45.32	-26.16	+5.02	-
20.0	-5.03	-0.69	-5.61	-57.69	+49.24	+76.35	-
21.0	-2.29	-2.01	+51.04	-112.23	+123.50	-261.33	-

Notes. The table gives $q_{jk}(G)$ at the values of G in the first column. For other values of G , linear interpolation should be used. A dash (–) indicates that the coefficient is zero. Units are: μas (for q_{0k}) and $\mu as \mu m$ (q_{1k}).

5. Comparison and verification

In this section, we apply the new bias correction in this work (TW) and the L21 correction to various samples to evaluate and compare their effectiveness. We use quasars, used for deriving the correction in Sect 4.1, to perform a consistency check on the procedures used to derive the correction. Additionally, we test two corrections on globular clusters and sources with independent parallaxes from other surveys or methods, which were independent of the derivation process.

5.1. Using quasars

We apply two bias corrections to quasars described in Sect 4.1, expecting the mean corrected parallaxes applying the new bias correction to be closer to zero, independent of magnitude, colour, etc. Figure 10 shows the results for the five-parameter solutions, divided according to magnitude, colour, and ecliptic latitude. Black circles show mean values of the uncorrected parallaxes (ϖ) in bins of magnitude etc.; blue circles and green circles show mean values of the corrected parallaxes ($\varpi - Z_5$) applying the new correction of this work (TW) and L21 correction respectively. Overall, the parallaxes corrected with the new bias correction are closer to zero than those corrected with the L21 model, indicating that the new correction is more applicable to the Galactic plane. The correction difference between L21 and

this work is approximately $9.71 \mu as$ at the faint magnitude end and go up to $11.07 \mu as$ when $v_{eff} = 1.42 \mu m^{-1}$.

5.2. Using globular clusters

Since all stars in a given globular cluster share the same true parallax (with negligible spread), we can use stars in globular clusters to validate bias corrections. Vasiliev & Baumgardt (2021) utilised GEDR3 data to investigate the kinematic properties of Milky Way globular clusters, employing a mixture modelling approach to simultaneously determine cluster membership probabilities for each star and infer cluster properties, particularly the mean parallax. Several clusters located at $|b| \leq 20^\circ$ are considered for our purpose, including NGC 6397, NGC 5139, NGC 6121, and NGC 6656. These clusters are located at $b \simeq -12^\circ$, $+15^\circ$, $+16^\circ$, and -8° , with mean parallaxes of 0.416 ± 0.010 mas, 0.193 ± 0.009 mas, 0.556 ± 0.010 mas, and 0.306 ± 0.010 mas (Vasiliev & Baumgardt 2021), respectively. We select stars in these clusters with five-parameter solutions that have high membership probability and reliable astrometric measurements, as described in Eq. (7).

$$\begin{cases} (i) & qflag = 3, \\ (ii) & memberprob \geq 0.9 \end{cases} \quad (7)$$

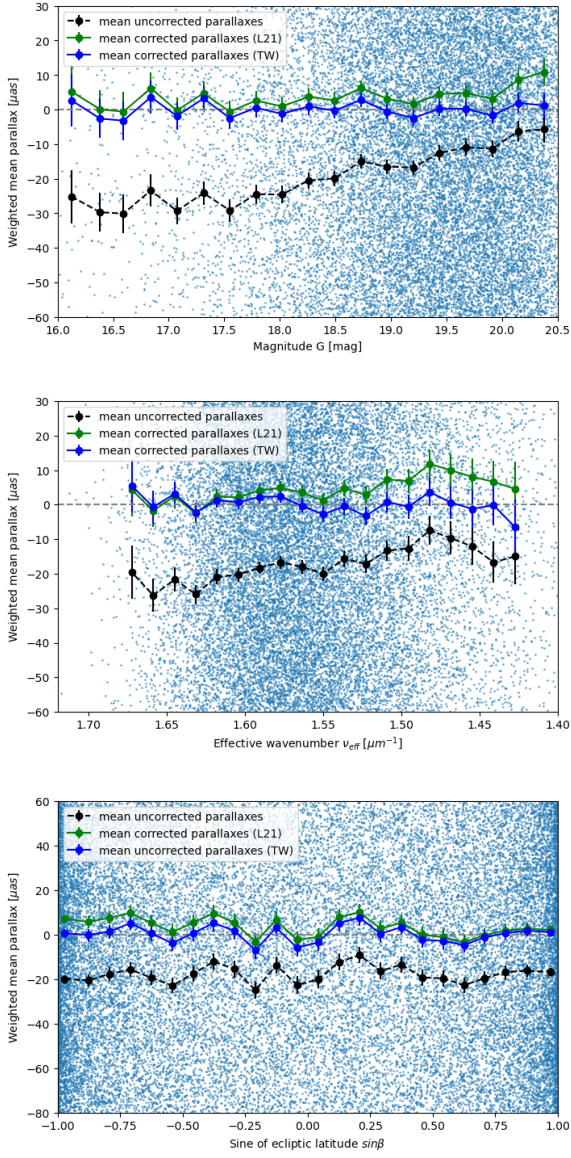


Fig. 10. Parallaxes for 180 231 quasars with five-parameter solutions in GDR3.

Criterion (i) selects reliable astrometric sources with five-parameter solutions; Criterion (ii) selects stars with high membership probability ($\geq 90\%$). Using these ‘clean’ subsets, we compare the validity of the two bias corrections.

Figure 11 shows the results for stars in NGC 6397, divided according to magnitude, effective wavenumber and ecliptic latitude. Blue dots show the individual values plotted versus magnitude, effective wavenumber, and sine of ecliptic latitude. Black circles show mean values of the uncorrected parallaxes (ϖ) in bins of magnitude etc.; blue circles and green circles show mean values of the corrected parallaxes ($\varpi - Z_5$) applying the new correction of this work (TW) and the L21 correction respectively. The middle grey dashed line indicates the mean parallax (0.416 mas), while the other two grey dashed lines represent its statistical uncertainty (0.010 mas). Overall, the corrected parallaxes applying the new correction are closer to the mean parallax. The correction difference of NGC 6397 between L21 and this work is about $10.0 \mu\text{as}$ when $0.9 < \sin\beta < 0.95$, and can go up to $17.82 \mu\text{as}$ when $G = 16$. Results for the other clusters are described in Sect. 5.4.

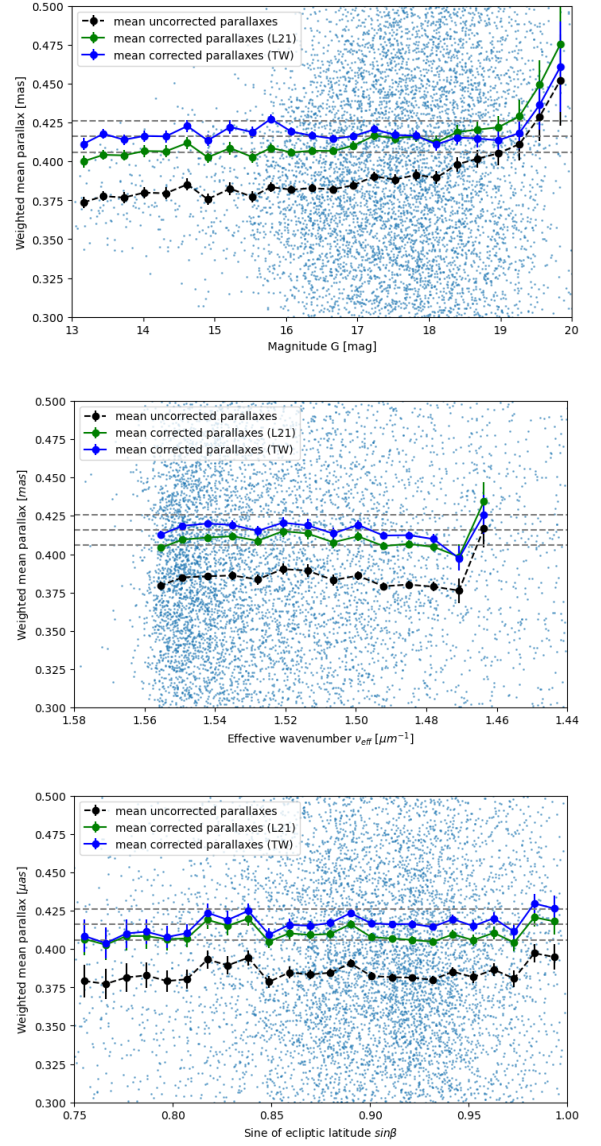


Fig. 11. Parallaxes for 12 307 stars in NGC 6397 with five-parameter solutions in GDR3.

5.3. Using sources with independent parallaxes from other surveys or methods

Following the method in Sect. 3.3, we compare independent parallaxes from other surveys or methods with the GDR3 parallaxes to assess the validity of the two corrections in the Galactic plane. VLBI, HST and RG sources with independent parallaxes, located at $|b| \leq 20^\circ$, are listed in Table 1. Since these sources may have different external systematics, their tests serve as secondary verification. The results are given in Table 6. The new correction in this work (TW) proves more effective than the L21 correction for VLBI sources. Other sources show comparable results for both two corrections. Overall, our correction demonstrates effectiveness for most sources with independent parallaxes.

5.4. Limitations

Results for NGC 5139, NGC 6121, and NGC 6656 can be found in Appendix D. Overall, the two corrections exhibit similar efficacy for these clusters, though the two corrections are not opti-

Table 6. Parallax corrections for sources with independent parallaxes located at $|b| \leq 20^\circ$ with five-parameter solutions.

Catalogue	$\Delta\varpi$ (uncorrected parallax offset) (μas)	L21 correction (μas)	TW correction (μas)	N
VLBI	-8.22	+21.48	+9.37	32
HST	-22.96	+1.43	+1.22	7
Red Giant	-19.15	+2.21	+2.30	6300

Notes. Column 1 gives the Name of catalogues. Column 2 gives the weighted mean of the offset between the observed GDR3 parallaxes and the independent parallaxes. Column 3 gives the weighted mean of the L21 correction. Column 4 gives the weighted mean of this work. Column 5 gives the number of sources located at $|b| \leq 20^\circ$ with five-parameter solutions.

mal. This may be due to challenges in determining globular cluster membership of Vasiliev & Baumgardt (2021). We acknowledge the possibility that our correction method may be sample-dependent. However, even with a more comprehensive sample for fitting the new model, sample dependence issues may persist (Groenewegen 2021).

6. Summary

L21 proposed a complex recipe to address parallax bias in GDR3, drawing from quasars in GCRF3, stars in LMC, and physical binaries. However, since the L21 sample is sparse in the Galactic plane, we evaluated the efficiency of the L21 correction in this region using quasars, wide binaries, and sources with parallaxes from other surveys or methods. Results, detailed in Fig. 4 - 7 and Table 2, suggest that the L21 correction is sample-dependent and not applicable to the Galactic plane. We fit the parallax bias function for sources with five-parameter solutions and get the new coefficients applying to the Galactic plane, primarily based on parameterised function $Z(G, v_{\text{eff}}, \beta)$ defined in L21 Appendix A. Direct estimation of the parallax bias via quasars is supplemented by indirect methods involving binaries. For sources in this region with five-parameter solutions in GDR3, the new fitted bias function is given by the functions $q_{jk}(G)$ obtained through linear interpolation in Table 5.

In this study, we present a new parallax bias correction tailored specifically for the Galactic plane, offering improvements over the existing L21 correction where the validity for the Galactic plane was untested. The correction difference between L21 and this work can go up to $10 \mu\text{as}$ within certain ranges of magnitude and colour. The differences in the results of the two corrections are mainly reflected in magnitude and colour, which may be caused by the influence of extinction on the Milky Way disk on the magnitude and colour. Historically, the Galactic plane has posed challenges for quasar surveys due to its high source density and significant extinctions. Our work represents a comprehensive effort to compile the most exhaustive collection of quasars within this region to date. It is important to note that our paper does not claim to provide a definitive solution, but rather offers a new approach to address the parallax bias issue in the Galactic plane. This work provides an additional recipe for users of *Gaia* parallaxes, especially for sources located near the Galactic plane. We acknowledge the possibility that our correction method may be sample-dependent. However, we have endeavoured to incorporate data from diverse sources within the Galactic plane and rigorously tested our correction against various samples. Further progress is expected with *Gaia* DR4, which will have improved parallax uncertainties and reduced systematics.

Acknowledgements. We appreciate the insightful advice provided by Dr. G.A. Brown. This work has made use of data from the European Space Agency

(ESA) mission *Gaia* (<https://www.cosmos.esa.int/gaia>), processed by the *Gaia* Data Processing and Analysis Consortium (DPAC, <https://www.cosmos.esa.int/web/gaia/dpac/consortium>). Funding for the DPAC has been provided by national institutions, in particular the institutions participating in the *Gaia* Multilateral Agreement. This research has made use of the VizieR catalogue access tool and the cross-match service provided by CDS, Strasbourg. We are also very grateful to the developers of the TOPCAT (Taylor 2005) software. This work has been supported by the National Natural Science Foundation of China (NSFC) through grants 12173069, the Youth Innovation Promotion Association CAS with Certificate Number 2022259, the Talent Plan of Shanghai Branch, Chinese Academy of Sciences with No.CASSHB-QNPD-2023-016, the Strategic Priority Research Program of the Chinese Academy of Sciences, Grant No.XDA0350205. We acknowledge the science research grants from the China Manned Space Project with NO. CMS-CSST-2021-A12 and NO.CMS-CSST-2021-B10.

References

- Benedict, G. F., McArthur, B. E., Nelan, E. P., & Harrison, T. E. 2017, *PASP*, 129, 012001
- Bond, H. E., Nelan, E. P., Remage Evans, N., Schaefer, G. H., & Harmer, D. 2018, *ApJ*, 853, 55
- Casertano, S., Riess, A. G., Anderson, J., et al. 2016, *ApJ*, 825, 11
- Dias, W. S., Monteiro, H., Caetano, T. C., et al. 2014, *A&A*, 564, A79
- El-Badry, K., Rix, H.-W., & Heintz, T. M. 2021, *MNRAS*, 506, 2269
- Fabrizius, C., Luri, X., Arenou, F., et al. 2021, *A&A*, 649, A5
- Fu, Y., Wu, X.-B., Jiang, L., et al. 2022, *ApJS*, 261, 32
- Fu, Y., Wu, X.-B., Li, Y., et al. 2024, *ApJS*, 271, 54
- Fu, Y., Wu, X.-B., Yang, Q., et al. 2021, *ApJS*, 254, 6
- Gaia Collaboration, Bailer-Jones, C. A. L., Teyssier, D., et al. 2023a, *A&A*, 674, A41
- Gaia Collaboration, Brown, A. G. A., Vallenari, A., et al. 2018, *A&A*, 616, A1
- Gaia Collaboration, Klioner, S. A., Lindegren, L., et al. 2022, *A&A*, 667, A148
- Gaia Collaboration, Prusti, T., de Bruijne, J. H. J., et al. 2016, *A&A*, 595, A1
- Gaia Collaboration, Vallenari, A., Brown, A. G. A., et al. 2023b, *A&A*, 674, A1
- Groenewegen, M. A. T. 2021, *A&A*, 654, A20
- Hogg, D. W., Eilers, A.-C., & Rix, H.-W. 2019, *AJ*, 158, 147
- Huang, Y., Schönrich, R., Zhang, H., et al. 2020, *ApJS*, 249, 29
- Huang, Y., Yuan, H., Beers, T. C., & Zhang, H. 2021, *ApJ*, 910, L5
- Jin, J.-J., Wu, X.-B., Fu, Y., et al. 2023, *ApJS*, 265, 25
- Khan, S., Miglio, A., Willett, E., et al. 2023, *A&A*, 677, A21
- Kharchenko, N. V., Piskunov, A. E., Schilbach, E., Röser, S., & Scholz, R. D. 2013, *A&A*, 558, A53
- Liao, S., Wu, Q., Qi, Z., et al. 2021, *PASP*, 133, 094501
- Lindegren, L., Bastian, U., Biermann, M., et al. 2021a, *A&A*, 649, A4
- Lindegren, L., Klioner, S. A., Hernández, J., et al. 2021b, *A&A*, 649, A2
- Lyke, B. W., Higley, A. N., McLane, J. N., et al. 2020, *ApJS*, 250, 8
- Muraveva, T., Delgado, H. E., Clementini, G., Sarro, L. M., & Garofalo, A. 2018, *MNRAS*, 481, 1195
- Nakoneczny, S. J., Bilicki, M., Pollo, A., et al. 2021, *A&A*, 649, A81
- Reid, M. J. & Honma, M. 2014, *ARA&A*, 52, 339
- Ren, F., Chen, X., Zhang, H., et al. 2021, *ApJ*, 911, L20
- Riess, A. G., Casertano, S., Anderson, J., MacKenty, J., & Filippenko, A. V. 2014, *ApJ*, 785, 161
- Riess, A. G., Casertano, S., Yuan, W., et al. 2018, *ApJ*, 855, 136
- Souchay, J., Secrest, N., Sexton, R., & Barache, C. 2024, *A&A*, 683, A112
- Storey-Fisher, K., Hogg, D. W., Rix, H.-W., et al. 2024, *ApJ*, 964, 69
- Taylor, M. B. 2005, in *Astronomical Society of the Pacific Conference Series*, Vol. 347, *Astronomical Data Analysis Software and Systems XIV*, ed. P. Shopbell, M. Britton, & R. Ebert, 29
- van Belle, G. T., Schaefer, G. H., von Braun, K., et al. 2020, *PASP*, 132, 054201
- Vasiliev, E. & Baumgardt, H. 2021, *MNRAS*, 505, 5978
- Xu, S., Zhang, B., Reid, M. J., Zheng, X., & Wang, G. 2019, *ApJ*, 875, 114
- Zinn, J. C. 2021, *AJ*, 161, 214

Appendix A: ADQL queries for the galaxy and star sample

Figure 2 shows the distribution of the two colours of Non-GCRF3 quasars, GCRF3 quasars, galaxies, and stars located at $|b| \leq 20^\circ$. The sources used to construct samples of galaxies and stars are as follows:

- Galaxies: random 100 000 galaxies located at $|b| \leq 20^\circ$ using criteria provided in [Gaia Collaboration et al. \(2023a, see Table 11\)](#) to select the pure galaxy sample. The ADQL query is as follows.

```
SELECT TOP 100000 g.*
FROM gaiadr3.galaxy_candidates as c
INNER JOIN gaiadr3.gaia_source as g
USING (source_id)
WHERE (c.radius_sersic IS NOT NULL
OR c.classlabel_dsc_joint='galaxy'
OR c.vari_best_class_name='GALAXY')
AND (g.b BETWEEN -20 AND 20)
```

- Stars: We take a random 100 000 stars located at $|b| \leq 20^\circ$ by selecting high reliable astrometric sources which are not candidates of quasars and galaxies. The ADQL query is as follows.

```
SELECT TOP 100000 *
FROM gaiadr3.gaia_source
WHERE in_qso_candidates = 'false'
AND in_galaxy_candidates = 'false'
AND ruwe <= 1.4
AND parallax <= 0.2
AND parallax_over_error >= 5
AND astrometric_excess_noise_sig <= 2
AND astrometric_excess_noise <= 0.1
AND visibility_periods_used > 11
AND duplicated_source = 'false'
AND phot_variable_flag != 'VARIABLE'
AND phot_bp_mean_flux_over_error > 100
AND phot_g_mean_flux_over_error > 100
AND phot_rp_mean_flux_over_error > 100
AND b BETWEEN -20 AND 20
```

Appendix B: Parallax differences of binaries against magnitude and colour differences

Figure B.1 and B.2 show the results for the five-parameter solutions of WBs located at $|b| \leq 20^\circ$ and $|b| > 20^\circ$ according to magnitude difference ($G_1 - G_2$) and colour difference ($v_{eff1} - v_{eff2}$), respectively. The parallax differences go to zero for small magnitude and colour differences for both the corrected and uncorrected versions.

Appendix C: Parallax zero-point differences of sources with derived parallaxes against colour and ecliptic latitude

Figure C.1 shows the results for the five-parameter solutions of sources with derived parallaxes from different methods (RGs, RRLs, RCs, EWs, and RGBs), located at $|b| \leq 20^\circ$ (a) and $|b| > 20^\circ$ (b) according to colour and ecliptic latitude, respectively. VLBI and HST sources are not plotted due to their small sample sizes. Overall, the parallax differences show clear distinctions between regions within and outside the Galactic plane.

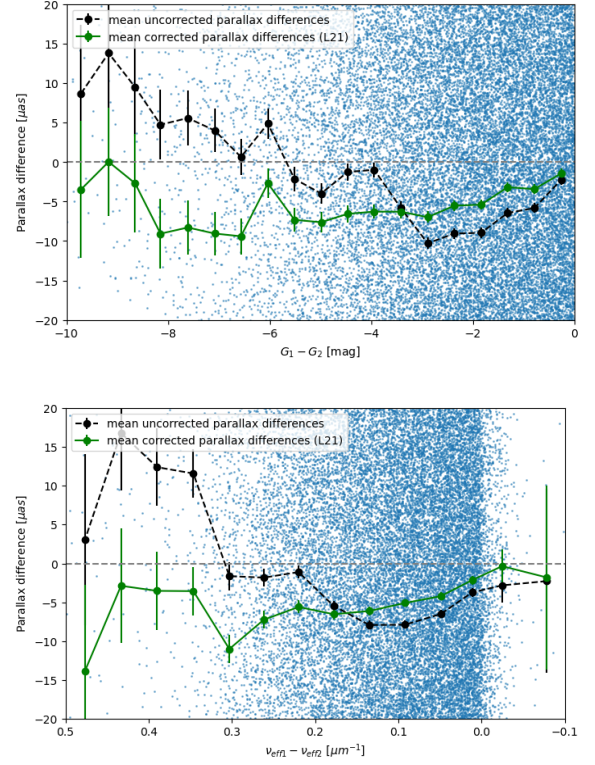


Fig. B.1. Parallax differences of 148 234 binaries located at $|b| \leq 20^\circ$ with five-parameter solutions versus magnitude and colour differences.

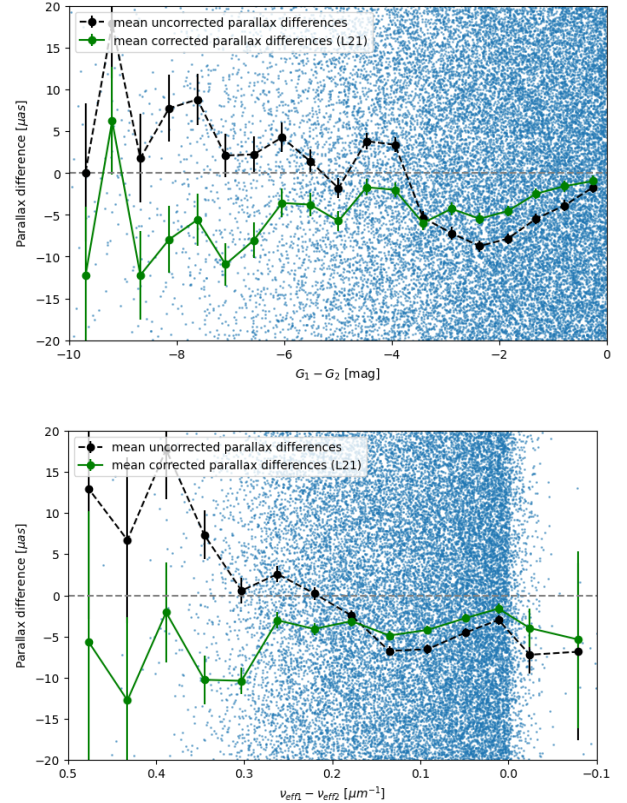


Fig. B.2. Parallax differences of 172 931 binaries located at $|b| > 20^\circ$ with five-parameter solutions versus magnitude and colour differences.

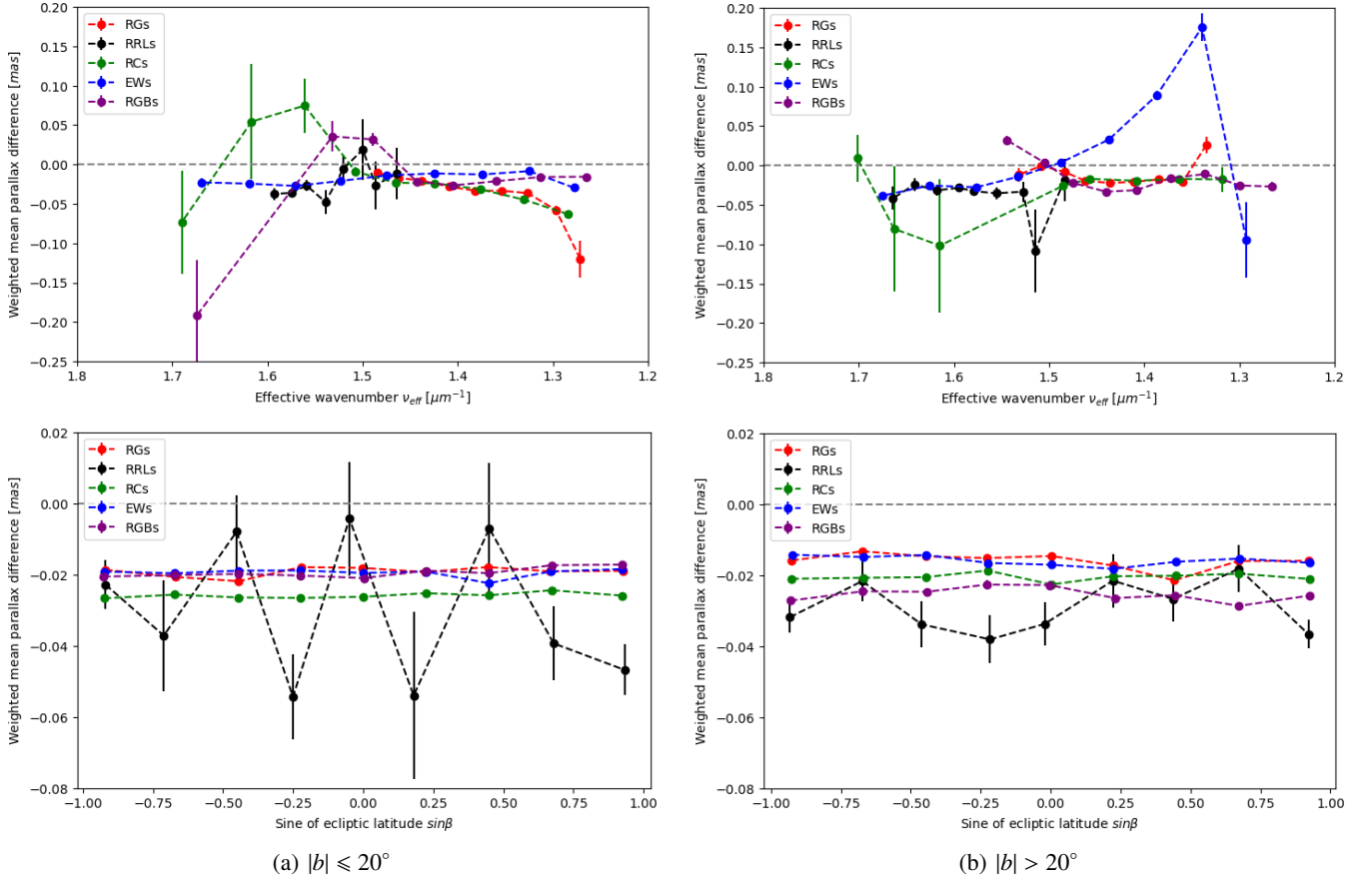


Fig. C.1. Parallax zero-point differences versus colour and ecliptic latitude of sources with derived parallaxes (RGs, RRLs, RCs, EWs, and RGBs) located at $|b| \leq 20^\circ$ (a) and $|b| > 20^\circ$ (b) with five-parameter solutions. The dots with error bars represent the weighted mean parallax differences for each bin across different samples. The large error bars for RRLs (black) are attributed to the limited sample size. The grey dashed line indicates a parallax difference of zero.

Appendix D: Tests of other globular clusters

Figure D.1, D.2, and D.3 show the results for stars in NGC 5139, NGC 6121, and NGC 6397, respectively. These figures are divided according to magnitude, effective wavenumber and ecliptic latitude. Blue dots show the individual values plotted versus magnitude, effective wavenumber, and sine of ecliptic latitude. Black circles show mean values of the uncorrected parallaxes (ϖ) in bins of magnitude etc.; blue circles and green circles show mean values of the corrected parallaxes ($\varpi - Z_5$) applying the new correction in this work (TW) and the L21 correction respectively. In Fig. D.1, the corrected parallaxes applying the L21 model (green) of NGC 5139 are closer to the mean parallax zone (0.193 ± 0.009 mas). Figures D.2 and D.3 show that both corrections yield comparable results within the well-populated region.

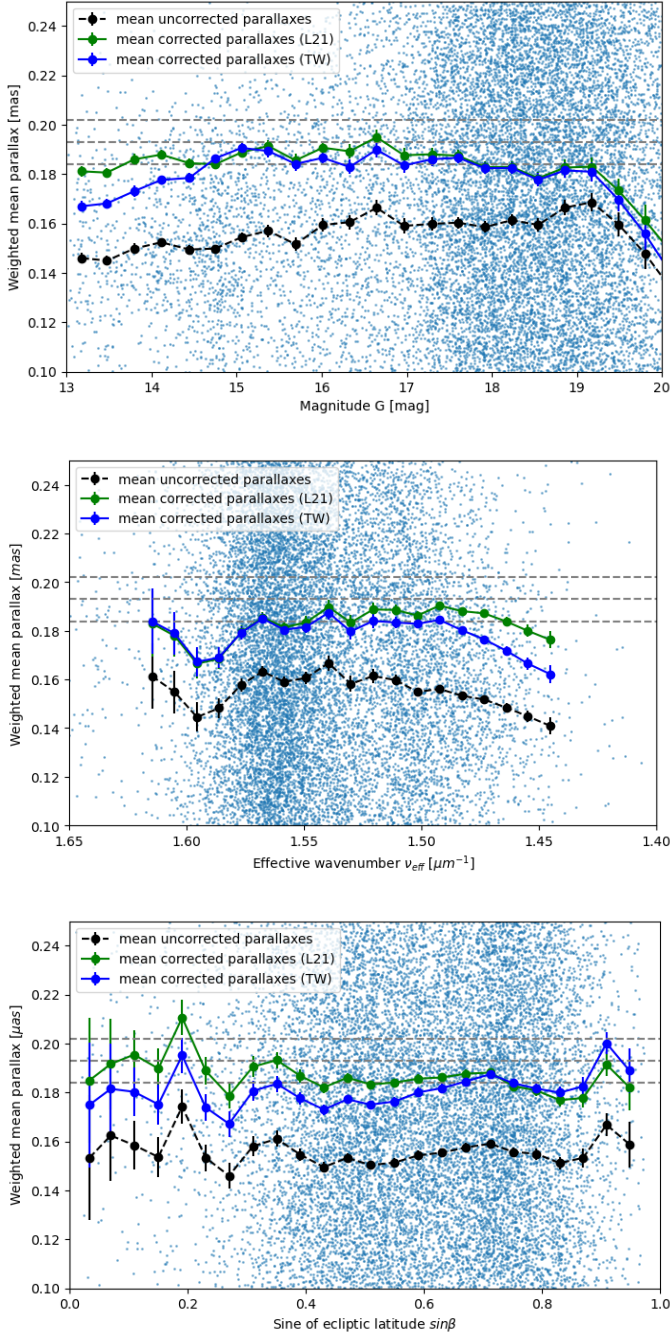


Fig. D.1. Parallaxes for 53 309 stars in NGC 5139 with five-parameter solutions in GDR3. The middle grey dashed line indicates the mean parallax (0.193 mas), while the other two grey dashed lines represent its statistical uncertainty (0.009 mas).

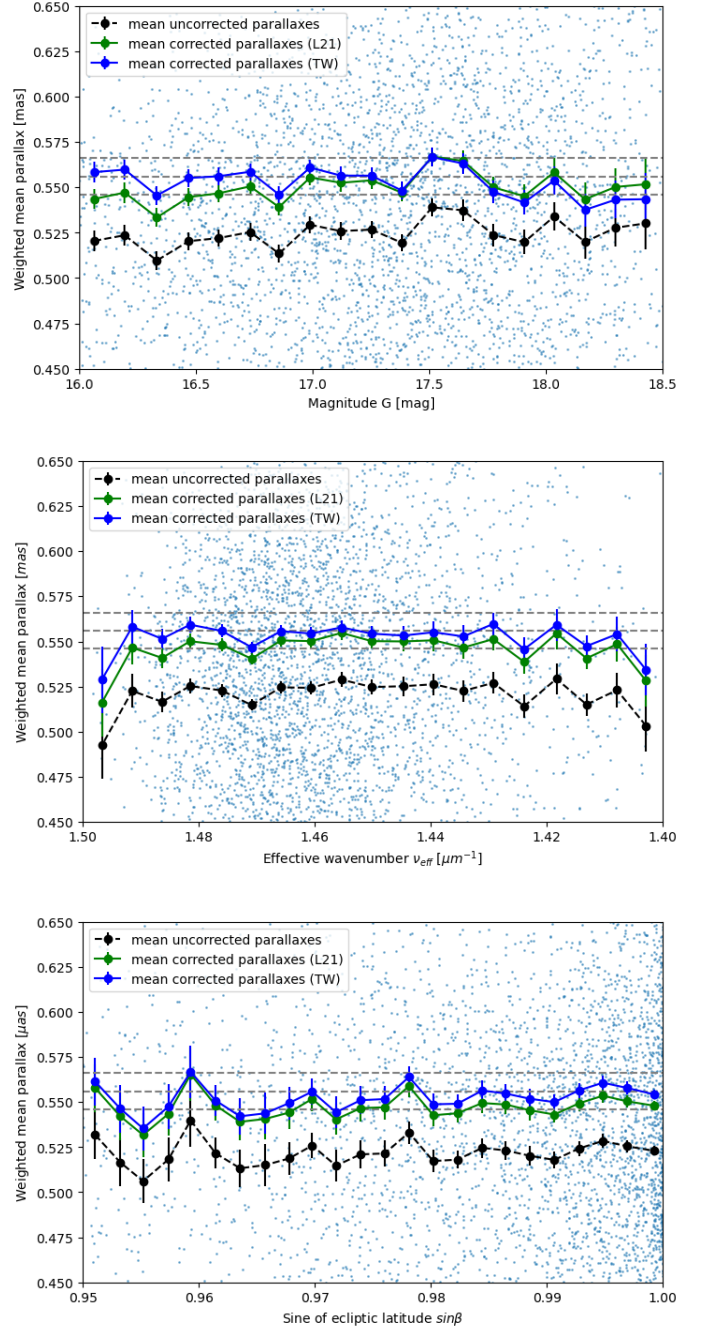


Fig. D.2. Parallaxes for 5208 stars in NGC 6121 with five-parameter solutions in GDR3. The middle grey dashed line indicates the mean parallax (0.556 mas), while the other two grey dashed lines represent its statistical uncertainty (0.010 mas).

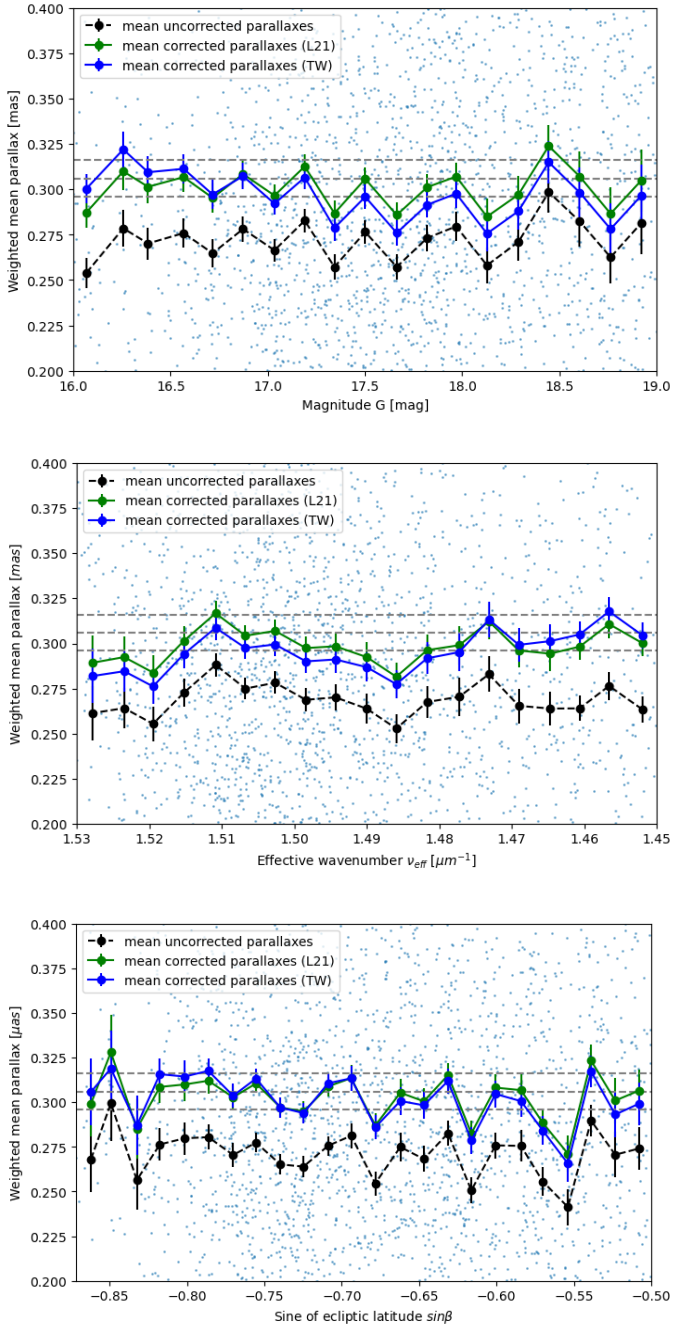


Fig. D.3. Parallaxes for 4323 stars in NGC 6656 (0.306 ± 0.010 mas) with five-parameter solutions in GDR3. The middle grey dashed line indicates the mean parallax (0.306 mas), while the other two grey dashed lines represent its statistical uncertainty (0.010 mas).